Free surface cusp formation as a failure mechanism for hard disk drives with fluid dynamic bearings

J. Billingham, P. Dellar, P. Evans, M. Hameed, R. Hinch, F. Hendriks,
T. Marchant, S. Patel, B. Tilley, D. Tselulko

August 30, 2004

1   Introduction

It is an acknowledged fact that ball bearing spindles of hard disk drives (HDD) are rapidly being replaced by spindles using fluid dynamic bearings (FDB) [**?**]. Some of the reasons are that FDBs offer superior non-repeatable runout (NRRO) and quieter operation. During operation the rotating part (rotor) of the HDD is supported by pressures created in a thin oil film without solid/solid contact. The oil film pressures are usually c created by slanted grooves in either the rotor or the stator: the part of the spindle that stands still. Several different FDB designs exist. We limit ourselves to the study of radial (also called journal) bearings in which the shaft is stationary and does not have any grooves, while the rotor has grooves in the shape of a "herringbone" - a series of repeated V-grooves. The orientation of the V-grooves is such that oil pressure builds-up at the apex of the V. The herringbone grooves can be considered an oil pump which generates pressure, but no flow. Each FDB holds a few milligrams of carefully formulated oil. The oil must satisfy many requirements, not the least of which is to stay in the FDB. When the disks do not spin, the oil is held in the FDB by capillary pressures alone. When the disks spin the location of the oil is dominated by fluid dynamic pressures in the FDB. In some FDB designs one or more of the oil-air boundaries are located in the grooved region of the FDB. This is cause for concern because the grooves disturb the oil-air interface. When this disturbing effect is strong enough small air bubbles can enter the oil, as described by Asada[2]. Once air bubbles are in the FDB they affect the stiffens and damping of the rotor dynamical system composed of the rotor and stator. Every HDD relies on an extremely precise servo feedback control system that can keep the read/write head over magnetically written tracks within an error of a few percent of the track width, which is itself a few tenths of a micron. Despite the considerable bandwidth of the servo system some disturbances to the servo-mechanical system happen on a time scale short enough to cause errors. Among these disturbances are such things as externally imposed vibration and internal sources of vibration such as air turbulence in the HDD and rapid, transient events in the FDB. Our main goal is to study how the oil-air interface behaves when it is located in the groove pattern of a radial (journal) bearing. Table 1 shows typical running conditions of a high-performance server drive and non-dimensional fluid dynamic parameters that govern the nature of the capillary flow in the FDB. Figure 1 shows a complete journal (A to B) and thrust bearing (B to C) (TSD stands for "tied-shaft" design). TSD-detail shows the coupled thrust-journal bearing and its capillary interfaces. When the rotor R spins around the stationary shaft S the location of the oil air interfaces moves to equilibrium positions different from the locations with the spindle at rest. the journal clearance d is of the order of a few microns. The distance L is typically a few mm. Note that one side of the herringbone pattern HB is longer than the other. This allows the thrust bearing to balance the pressure created by the radial bearing. In this paper we restrict our attention to the upper herringbone region of axial length L.

Figure 2 is a fluid model (not solid) of the oil in the combined radial-thrust bearing. All lubrication gaps have been vastly exaggerated to make the grooves visible. Groove gaps tend to be a few micron thicker than clearance gaps. Figure 1 and the values in Table 1 show clearly that the flow is of Hele-Shaw type. What is

Dimensional quantities		Dimensionless quantities	
Gap thickness d	10 μm	Aspect Ratio	$\epsilon = d/r_i = 10^{-3}$
Stator radius/height r_i, L	2 mm	Ekman Number	$E = \nu/(\Omega r_i^2) \sim 10^{-3} - 10^{-4}$
Rotation rate Ω	15,000 rpm	Reynolds Number	$Re = \rho \Omega r_i d/\mu = 6.6$
Fluid density ρ	885 kg/m^3	Froude Number	$Fr = (\Omega r_i)^2/(gd) = 9.2 \times 10^5$
Fluid dynamic viscosity μ	0.004 Pa· s	Capillary Number	$Ca = \mu \Omega r_i/\sigma = 0.6$
Surface tension σ	0.02 N/m	Bond Number	$Bo = \rho g d^2/\sigma = 4 \times 10^{-7}$

Table 1: Table of dimensional and dimensionless quantities.

unusual in this case is the strong shear of the flow. The high shear causes complex secondary flows in the grooved geometry which interact with the free surface. We are curious to investigate whether strong surface deformation could give rise to phenomena such as tip streaming.

A Hele-Shaw cell is made of two parallel plates, placed at a short distance, between which there is slow flow of a viscous liquid, (see [8, 10], and [16]). When a Hele-Shaw cell is filled partially with a fluid, then the interface is prone to fingering instabilities. Between the dendritic structures is a cusp-like region, and the mathematical description of this region has been the subject of debate. The standard mathematical treatment involves a Darcy flow within the liquid, and a depth-averaged version of the kinematic boundary condition. However, this model is ill-posed, and various techniques have been used to regularize the problem, from including miscibility to including higher-order capillary effects. Mathematical interest in the degree of the singularity has also been of interest (for more information, see [1, 5, 7, 9, 13, 12, 11, 15, 16, 18, 19, 20, 23, 24]). Various extensions in geometries and temporal forcing has also been investigated, including varying the gap width temporally (see [6] and [22]) and rotating about an axis normal to the plates (see [3]),

In the following, we show that the fluid dynamic bearing resembles a Hele-Shaw cell with differential motion of the plates. We derive a Reynolds equation that describes the pressure between the stator and the rotor, assuming that the gradient in the gap width due to the herringbone pattern is small. This equation is coupled to the motion of the interface through the kinematic boundary condition. From this, we consider a linear and weakly nonlinear analysis of the system. We find that the physical effects of rotation, surface tension, and inertia are negligible over the relevant time scales. Two independent numerical simulations of the coupled systems are performed next, which confirm the linear theory and shows the potential for cusp formation along the interface after a time comparable to the rotation period.

The report is organized as follows. We describe the asymptotic approach to the Reynolds equation in Section 2. Section 3 investigates the solutions for small variations in the gap thickness. Section 4 investigates these equations numerically, and a numerical investigation for extending this work to more sharply etched grooves is presented. We conclude in Section 5.

2   Problem Description

Consider the motion of an incompressible viscous fluid between the stator and rotor as shown in Figure 3. We use a cylindrical polar coordinate system centered at the stator, but a rotating frame of reference in with the *rotor* appears fixed. The stator then appears to rotate backwards in this frame, in which the continuity and Navier-Stokes equations are

$$\nabla \cdot \mathbf{u}^* \ = \ 0 \tag{1}$$

$$\rho \frac{D\mathbf{u}^*}{Dt} \ = \ -\nabla p^* + \mu \nabla^2 \mathbf{u}^* - 2\rho \Omega \mathbf{k} \times \mathbf{u}^* - \rho \Omega^2 r \mathbf{r}. , \tag{2}$$

where $\mathbf{r}, \mathbf{k}$ are the unit vectors in the radial and axial directions, respectively. The last two terms in (2) are the Coriolis and centrifugal forces due to the rotating reference frame. These equations hold in the region
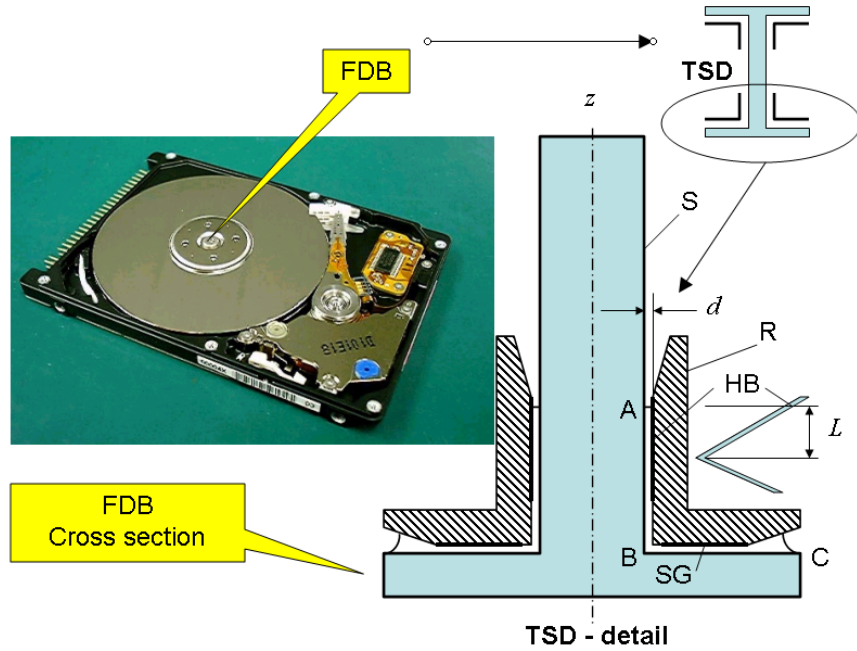
Figure 1: Characteristic disk drive, with the red box showing the location of the motor. Right: Side view schematic of the motor unit with the spindle, the rotor, and the fluid bearing.
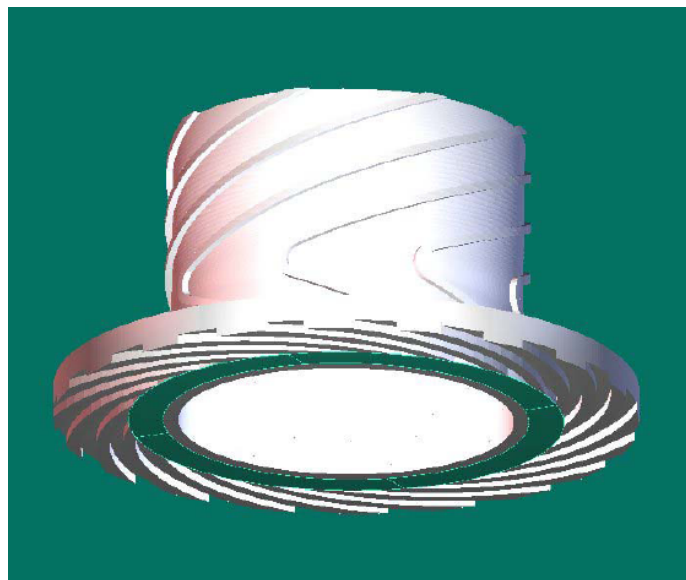
Figure 2: Characteristic spindle with herringbone pattern viewed on the cylindrical shell. The depth is enhanced to show the pattern, and is not to scale with the true physical depth.
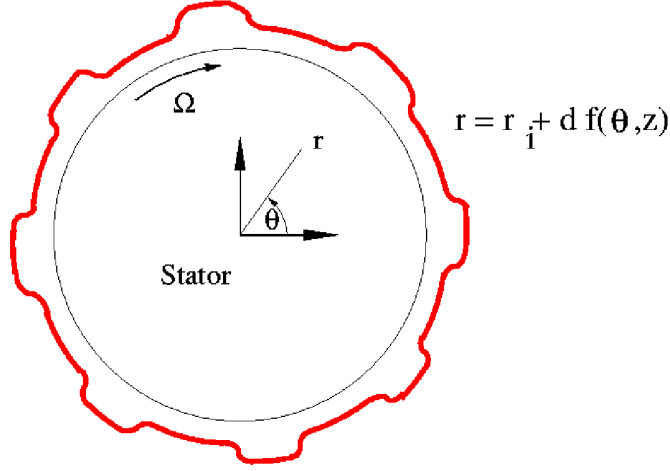
Figure 3: Rotating coordinate frame to be used in the derivation. Note that the rotor is rotating with angular velocity Ω in the positive θ direction with respect to an inertial frame. The analysis that follows is in the frame of the rotor, in which the stator appears to rotate backwards.

$r_i < r < r_i + d\,f(\theta, z)$, $0 < z < Z(r, \theta, t)$ and $0 < \theta < 2\pi$. Here $\mathbf{u}^* = (u_r^*, u_\theta^*, u_z^*)$ is the fluid velocity, with components in the radial, azimuthal, and axial directions (r, θ, z) respectively, and p^* is the fluid pressure[1]. ρ is the fluid density, μ is the dynamic viscosity, and Ω is the applied rotation rate. The velocity must satisfy no-slip boundary conditions at the inner and outer walls. Thus $(u_r^*, u_\theta^*, u_z^*) = (0, -\Omega r_i, 0)$ at $r = r_i$ on the stator, while $\mathbf{u}^* = \mathbf{0}$ at $r = r_i + d\,f(\theta, z)$ on the rotor. As suggested by figure 2, we assume the following symmetry conditions hold on the centerline $z = 0$,

$$\frac{\partial u_\theta^*}{\partial z} = \frac{\partial u_r^*}{\partial z} = u_z^* = \frac{\partial p^*}{\partial z} = 0 \ .$$

Along the fluid interface $z = Z^*(r, \theta, t)$, we impose the usual kinematic boundary condition, that normal fluid stresses balance capillary stress, and that the shear stress vanish

$$\frac{\partial Z^*}{\partial t} \quad + \quad \mathbf{u}^* \cdot \mathbf{n} = 0 \tag{3}$$

$$\sigma \kappa^* \quad = \quad p^* - \mathbf{n} \cdot \mathbf{T}^* \cdot \mathbf{n} \tag{4}$$

$$[\mathbf{n} \cdot \mathbf{T}^*] \times \mathbf{n} \quad = \quad 0 \ . \tag{5}$$

Here σ is the surface tension, κ^* equals twice the mean curvature, and $\mathbf{T}^* = \mu[\nabla \mathbf{u} + (\nabla \mathbf{u})^\mathsf{T}]$ is the viscous stress.

Since the gap thickness $d \ll r_i$, the fluid quantities are expected to primarily depend upon the reduced coordinate $r - r_i$ rather than the radial coordinate. We define the dimensionless coordinate $y = (r - r_i)/r_i$ as the radial coordinate in our system, we scale z on r_i, velocities on $U = \Omega r_i$, time on $1/\Omega$, and pressure on $\mu \Omega r_i^2/d^2$ to arrive at a dimensionless version of (1),

$$\frac{1}{1 + \epsilon y} \frac{\partial}{\partial y} \{(1 + \epsilon y) u_r\} + \frac{\epsilon}{1 + \epsilon y} \frac{\partial u_\theta}{\partial \theta} + \epsilon \frac{\partial u_z}{\partial z} \quad = \quad 0 \ . \tag{6}$$

From this relation, $u_r = \epsilon u_y, u_y = O(1)$ to balance the terms in this equation. This then results in the

---

[1]Quantities denoted with an asterisk denote a dimensional quantity.

following radial, azimuthal, and axial components of the momentum equation,

$$\epsilon^2 \left\{ \frac{\partial u_y}{\partial t} + u_y \frac{\partial u_y}{\partial y} + \frac{u_\theta}{1+\epsilon y} \frac{\partial u_y}{\partial \theta} + u_z \frac{\partial u_y}{\partial z} \right\} - \frac{\epsilon u_\theta^2}{1+\epsilon y} = -\frac{E}{\epsilon} \frac{\partial p}{\partial y} + E \left\{ \frac{1}{1+\epsilon y} \frac{\partial}{\partial y} \left[(1+\epsilon y) \frac{\partial u_y}{\partial y} \right] \right.$$

$$\left. + \epsilon^2 \left[\frac{1}{(1+\epsilon y)^2} \frac{\partial^2 u_y}{\partial \theta^2} + \frac{\partial^2 u_y}{\partial z^2} - \frac{u_y}{1+\epsilon y} \right] - \frac{2\epsilon}{(1+\epsilon y)^2} \frac{\partial u_\theta}{\partial \theta} - \right\} + 2\epsilon u_y + 1 + \epsilon y \tag{7}$$

$$\epsilon^2 \left\{ \frac{\partial u_\theta}{\partial t} + u_y \frac{\partial u_\theta}{\partial y} + \frac{u_\theta}{1+\epsilon y} \frac{\partial u_\theta}{\partial \theta} + u_z \frac{\partial u_\theta}{\partial z} + \frac{u_y u_\theta}{1+\epsilon y} \right\} = \frac{E}{1+\epsilon y} \frac{\partial p}{\partial \theta} + E \left\{ \frac{1}{1+\epsilon y} \frac{\partial}{\partial y} \left[(1+\epsilon y) \frac{\partial u_\theta}{\partial y} \right] \right.$$

$$\left. + \epsilon^2 \left[\frac{1}{(1+\epsilon y)^2} \frac{\partial^2 u_\theta}{\partial \theta^2} + \frac{\partial^2 u_\theta}{\partial z^2} - \frac{u_\theta}{(1+\epsilon y)^2} \right] + \frac{2\epsilon^3}{(1+\epsilon y)^2} \frac{\partial u_y}{\partial \theta} \right\} - \epsilon u_y \tag{8}$$

$$\epsilon^2 \left\{ \frac{\partial u_z}{\partial t} + u_y \frac{\partial u_z}{\partial y} + \frac{u_\theta}{1+\epsilon y} \frac{\partial u_z}{\partial \theta} + u_z \frac{\partial u_z}{\partial z} \right\} = -E \frac{\partial p}{\partial z} + E \left\{ \frac{1}{1+\epsilon y} \left[(1+\epsilon y) \frac{\partial u_z}{\partial y} \right] \right.$$

$$\left. + \epsilon^2 \left[\frac{1}{(1+\epsilon y)^2} \frac{\partial^2 u_z}{\partial \theta^2} + \frac{\partial^2 u_z}{\partial z^2} \right] \right\} , \tag{9}$$

where $E = \nu/(\Omega r_i^2)$ is the Ekman number of the flow, or equivalently, the reciprocal of the Reynolds number using Ωr_i as the velocity scale. Sometimes the Taylor number $Ta = E^{-2}$ is used instead..

The corresponding boundary conditions at the centerline $z = 0$ are

$$\frac{\partial u_y}{\partial z} = \frac{\partial u_\theta}{\partial z} = u_z = \frac{\partial p}{\partial z} = 0 ,$$

and the interfacial conditions (3)-(5) become

$$\frac{\partial Z}{\partial t} = u_z - \frac{1}{1+\epsilon y} u_\theta \frac{\partial Z}{\partial \theta} - u_y \frac{\partial Z}{\partial y} \tag{10}$$

$$\frac{\epsilon}{Ca} \kappa = p - \frac{\epsilon}{Ca} \mathbf{n} \cdot \mathbf{T} \cdot \mathbf{n} \tag{11}$$

$$[\mathbf{n} \cdot \mathbf{T}] \times \mathbf{n} = 0 , \tag{12}$$

where κ is twice the (dimensionless) mean curvature.

Following the standard derivation of the Reynolds equation, we assume an asymptotic form for the velocities and the pressure

$$u_y = u_{yo} + \epsilon u_{y1} + \cdots$$
$$u_\theta = u_{\theta o} + \epsilon u_{\theta 1} + \cdots$$
$$u_z = u_{zo} + \epsilon u_{z1} + \cdots$$
$$p = p_o + \epsilon p_1 + \cdots .$$

At leading order, $p_o = p_o(\theta, z, t)$ from the y-momentum equation. The θ and z components of the momentum equation result in the equations

$$\frac{\partial^2 u_{\theta o}}{\partial y^2} = \frac{\partial p_o}{\partial \theta}$$

$$\frac{\partial^2 u_{zo}}{\partial y^2} = \frac{\partial p_o}{\partial z} ,$$

subject to the boundary conditions $u_\theta = -1, u_z = 0$ along $y = 0$, and $u_\theta = u_z = 0$ along $y = f(\theta, z)$. The solution results in a Couette–Poiseuille flow profile

$$u_{\theta o} = \frac{1}{2} \frac{\partial p_o}{\partial \theta} y(y - f(\theta, z)) - 1 + \frac{y}{f(\theta, z)} \tag{13}$$

$$u_{zo} = \frac{1}{2} \frac{\partial p_o}{\partial z} y(y - f(\theta, z)) . \tag{14}$$

5

Applying the continuity equation (6) and requiring that $u_{yo} = 0$ on both $y = 0$ and $y = f(\theta, z)$ results in the following Reynolds equation for the leading-order pressure (dropping the subscript)

$$\frac{\partial}{\partial \theta}\left\{f^3\frac{\partial p}{\partial \theta} + 6f(\theta, z)\right\} + \frac{\partial}{\partial z}\left\{f^3\frac{\partial p}{\partial z}\right\} = 0 \ . \tag{15}$$

Note that this solution does not include information about the interface. This formulation is valid provided that the velocity varies more slowly in the azimuthal and axial direction than in the radial direction. This assumption may be violated near the interface. However, we note that our scaling of the pressure as $\mathcal{O}(\mu\Omega r_i^2/d^2)$ implies that $p \to 0$ as $z \to Z(r, \theta, t)$. If a boundary-layer analysis is performed local to the interface (rescaling of z within a gap's width of the interface so that y and z-variations in the velocity are comparable), the result is a two-dimensional boundary layer system in terms of u_y, u_z, which is coupled to the azimuthal Couette flow. However, from Hele-Shaw flows, this boundary layer is typically passive: flows within the layer do not change the qualitative nature of the dynamics, and only vary at higher-order quantitatively[10]. Hence we assume that there is no boundary layer at the interface, and prescribe the flow velocities found above at the interfacial location. To form the appropriate pressure and kinematic conditions at the interface, we can apply a Galerkin expansion in the radial coordinate (see the Appendix for details), and keep only a finite number of terms. In Hele-Shaw flow, only the leading-order term is retained from this averaging , and the resulting condition on the interface is

$$\frac{\partial Z}{\partial t} + \bar{u}_\theta\frac{\partial Z}{\partial \theta} - \bar{u}_z = 0 \tag{16}$$

where $Z = Z(\theta, t)$ is the average interfacial height of the interface, and $\mathbf{u} = (\bar{u}_\theta, \bar{u}_z)$ is given by

$$\mathbf{u} = -\frac{1}{12}f^2\nabla p - \frac{1}{2}\hat{\theta} \ , \tag{17}$$

where $\nabla = \frac{\partial}{\partial_\theta}\hat{\theta} + \frac{\partial}{\partial_z}\hat{\mathbf{z}}$. This averaging of the normal stress boundary condition results in zero pressure at the interface.

In summary, the equations of motion to consider here are given by

$$\frac{\partial}{\partial \theta}\left\{f^3\frac{\partial p}{\partial \theta} + 6f(\theta, z)\right\} + \frac{\partial}{\partial z}\left\{f^3\frac{\partial p}{\partial z}\right\} = 0 \tag{18}$$

$$\frac{\partial Z}{\partial t} - \left[\frac{1}{2} + \frac{f^2}{12}\frac{\partial p}{\partial \theta}\right]\frac{\partial Z}{\partial \theta} + \frac{f^2}{12}\frac{\partial p}{\partial z} = 0 \ , \tag{19}$$

subject to the conditions $\partial p/\partial z = 0$ along $z = 0$, $p = 0$ along $z = Z(\theta, t)$, and p and Z are 2π-periodic in θ. Note that these equations are ill-posed when the interface deflects significantly, as is found in Hele-Shaw flows. A regularizing term will be added in the numerical solutions that follow.

3   Linear Theory

To begin the analysis of the system (18, 19), we first consider the case where the depth of the grooves are small compared with the mean gap thickness, which is already small compared with the radius. Consider

$$f(\theta, z) = 1 + \delta\sin\left(n\left[\theta - kz\right]\right) \ , \tag{20}$$

where $\delta \ll 1$ is the amplitude of the variation of the rotor walls, n is the number of grooves per circumference, and $k = \cot\alpha$, where α is the groove angle. Note that equation (18) is linear in the pressure, so that any variations in pressure are directly proportional to the groove depth. With this, we now consider a linearized version of (18,19) about the constant solution $p = 0, Z = 1$, given by

$$\nabla^2 p_o = -6n\cos\left(n[\theta - kz]\right) \tag{21}$$

6

$$\frac{\partial Z}{\partial t} - \frac{1}{2}\frac{\partial Z}{\partial \theta} + \frac{1}{12}\frac{\partial p_o}{\partial z} = 0 \ , \tag{22}$$

subject to the conditions $\frac{\partial p}{\partial z} = 0$ at $z = 0$, $p_o = 0$ at $z = 1$, and 2π periodicity in θ for p and Z. The solution of the leading-order pressure is

$$p_o = \frac{6}{n(1+k^2)}\left\{\cos\left[n\left(\theta - kz\right)\right] - \frac{\cos\left[n(\theta - k)\right]\cosh nz}{\cosh n} - \left[k\sinh nz - \frac{k\sinh n\cosh nz}{\cosh n}\right]\sin n\theta\right\} \ . \tag{23}$$

In figure 4, we show a sample pressure profile for the case $k = 2$, and for $n = 5, 10, 15$. Note that the amplitude of the pressure decreases for increasing n, as expected from (23). However, for larger values of k, large variations in the pressure gradient are localized near the centerline $z = 0$. This can be seen in figure 5, where $k = 10$ (or a groove angle of nearly 6°).

From this pressure field, the linearized interfacial deflection described in (22) is found directly to be

$$\begin{aligned}
Z_o(\theta, t) & = & Z_{in}\left(\theta + \frac{t}{2}\right) \\
& & -\frac{1}{n(1+k^2)\cosh n}\left\{\sinh n\sin\left[n(\theta - k)\right] + k\cosh n\cos\left[n(\theta - k)\right] - k\cos n\theta\right\} \\
& = & Z_{in}\left(\theta + \frac{t}{2}\right) + Z_p(\theta)
\end{aligned} \tag{24}$$

where Z_{in} is the initial condition of the interfacial location, and the remaining terms result from the forcing due to the steady-state pressure distribution (23). The amplitude of this forced term is found to be

$$|Z_o|_{Z_{in}=0} = \frac{k}{n(1+k^2)}\operatorname{sech} n \ .$$

Hence, the forced interfacial deflections are reduced exponentially as the number of grooves increases while they are reduced algebraically as the groove angle decreases.

An initial weakly nonlinear analysis is presented in the Appendix.

4 Numerical Approaches

4.1 Slowly Varying Groove Thickness

4.1.1 Model

From (17), the first term is a Poiseuille flow driven by the pressure gradient, while the second term is a Couette flow in the $-\theta$ direction driven by the differential rotation of the cylinders. This flow is backwards as seen in a frame rotating with the outer cylinder.

For future convenience, equation (18) may be rearranged into

$$\nabla\cdot(f^3\nabla p) = f^3\nabla^2 p_o + 3f^2\nabla f\cdot\nabla p = 6\frac{\partial f}{\partial\theta}. \tag{25}$$

Although equations (25) and (19) are both linear in p, the system as a whole is nonlinear due to the free boundary at $z = Z(\theta, t)$. Moreover, the domain for the elliptic equation (25) must be determined as part of the solution. The computation becomes much easier after eliminating the free boundary. Introducing the new vertical coordinate

$$\eta = \frac{z}{Z(\theta, t)}, \tag{26}$$
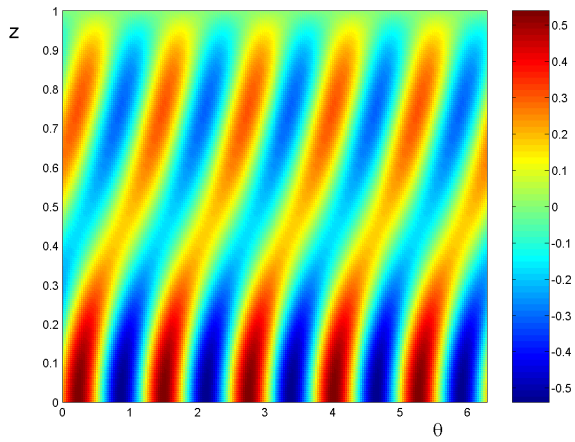
(a)
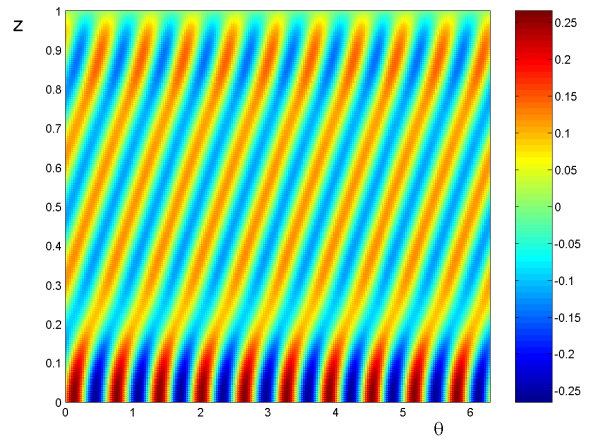
(b)
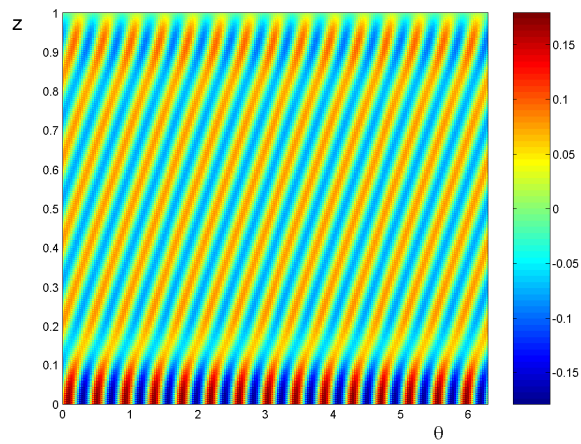
(c)

Figure 4: Pressure distribution over one azimuthal period for the wall profile $f(\theta, z) = 1 + \delta \sin\left[n(\theta - kz)\right]$ for $k = 2$ and for (a) $n = 5$, (b) $n = 10$, and (c) $n = 15$.
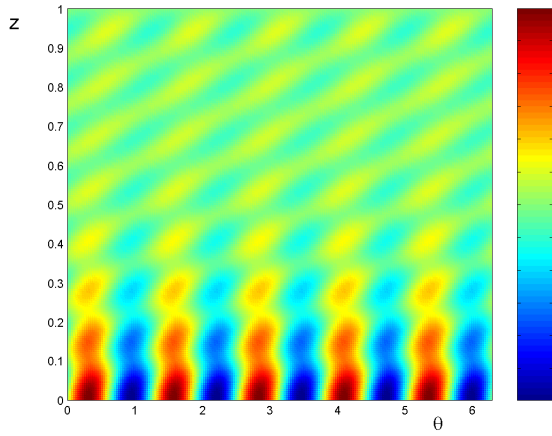
(a)
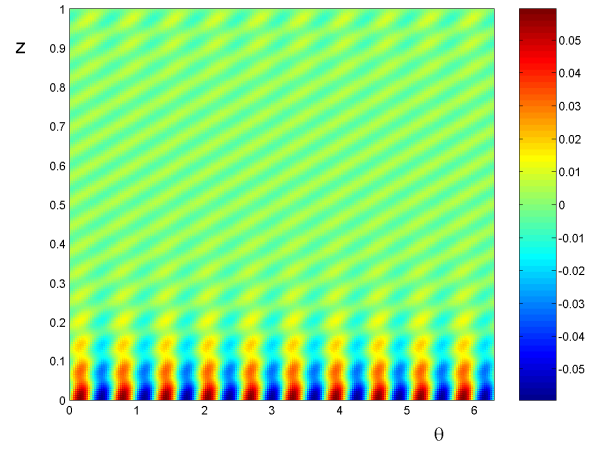
(b)
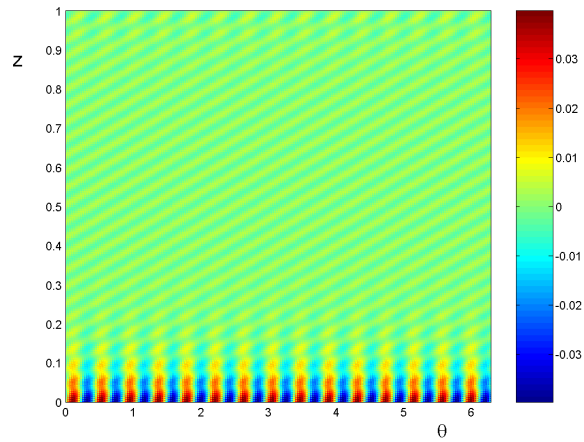
(c)

Figure 5: Pressure distribution over one azimuthal period for the wall profile $f(\theta, z) = 1 + \delta \sin[n(\theta - kz)]$ for $k = 10$ and for (a) $n = 5$, (b) $n = 10$, and (c) $n = 15$. Note that other than a localized region near $z = 0$, the pressure distribution remains relatively uniform over most of the height of the fluid.

9

maps the previous domain $0 \leq z \leq Z(\theta, t)$ to the strip $0 \leq \eta \leq 1$. Since $0 \leq \theta < 2\pi$ the new domain is a rectangle with periodic boundary conditions in θ. The resulting (θ, η) coordinate system is not orthogonal, so partial derivatives transform according to

$$\left.\frac{\partial}{\partial z}\right|_\theta = \frac{1}{Z}\left.\frac{\partial}{\partial \eta}\right|_\theta, \quad \left.\frac{\partial}{\partial \theta}\right|_z = \left.\frac{\partial}{\partial \theta}\right|_\eta - \eta\frac{Z_\theta}{Z}\left.\frac{\partial}{\partial \eta}\right|_\theta. \tag{27}$$

Since the grooves are fixed in the physical (θ, z) coordinates it makes sense to leave the derivatives of the gap thickness f expressed in (θ, z) coordinates. Equation (25) then becomes

$$f^3 \left[\left.\frac{\partial}{\partial \theta}\right|_\eta \left(\left.\frac{\partial p}{\partial \theta}\right|_\eta - \eta\frac{Z_\theta}{Z}\left.\frac{\partial p}{\partial \eta}\right|_\theta\right) - \frac{\partial Z}{\partial \theta}\left.\frac{\partial}{\partial \theta}\right|_\eta \left(\frac{\eta}{Z}\left.\frac{\partial p}{\partial \eta}\right|_\theta\right) + \left(1 + \eta^2\frac{\partial Z}{\partial \theta}^2\right)\frac{1}{Z^2}\left.\frac{\partial^2 p}{\partial \eta^2}\right|_\theta\right]$$

$$+3f^2\left.\frac{\partial f}{\partial \theta}\right|_z \left(\left.\frac{\partial p}{\partial \theta}\right|_\eta - \eta\frac{Z_\theta}{Z}\left.\frac{\partial p}{\partial \eta}\right|_\theta\right) + 3f^2\left.\frac{\partial f}{\partial z}\right|_\theta\frac{1}{Z}\left.\frac{\partial p}{\partial \eta}\right|_\theta = 6\left.\frac{\partial f}{\partial \theta}\right|_z, \tag{28}$$

while the kinematic free surface condition (19) becomes

$$\begin{aligned}
\frac{\partial Z}{\partial t} &= -\frac{1}{12}f^2\frac{\partial p}{\partial z} + \left(\frac{1}{12}f^2\frac{\partial p}{\partial \theta} + \frac{1}{2}\right)Z_\theta, \\
&= -\frac{1}{12}f^2\frac{1}{Z}\left.\frac{\partial p}{\partial \eta}\right|_\theta + Z_\theta\left[\frac{1}{2} + \frac{1}{12}f^2\left(\left.\frac{\partial p}{\partial \theta}\right|_\eta - \frac{Z_\theta}{Z}\left.\frac{\partial p}{\partial \eta}\right|_\theta\right)\right], \\
&= \frac{1}{2}Z_\theta - \frac{1}{12}f^2\frac{1+Z_\theta^2}{Z}\left.\frac{\partial p}{\partial \eta}\right|_\theta, \tag{29}
\end{aligned}$$

after noting that $\partial_\theta p = 0$ at constant η, since $p = 0$ along the free surface $\eta = 1$.

4.1.2 Numerical procedure

Equation (28) is a linear elliptic equation for p in a rectangular domain. The spatial coordinates were discretised using Fourier series in θ and second order centered differences in η. The resulting linear system of algebraic equations is not symmetric, because the different boundary conditions at $\eta = 0, 1$ make the original boundary value problem not self-adjoint. We therefore used the iterative Krylov space method known as generalised minimum residual (GMRES) [21] that is able to solve asymmetric linear systems. One subtlety is that the discretised differential equation only involves the pressure at $N_z - 1$ vertical grid points for each Fourier mode. The remaining equation ensures that the pressure at points on the free surface $\eta = 1$ takes its prescribed value, which we include as part of the right hand side. Although this value is zero for the model described above, it is nonzero for the regularised model with finite surface tension. GMRES was preconditioned using solutions of Poisson's equation with the same domain and boundary conditions. The different Fourier modes decouple, and solving Poisson's equation for each mode just requires the solution of the tridiagonal system of equations that arises from the centered finite differences in η.

Given the above algorithm to compute $p(\theta, \eta)$ from the known geometry $f(\theta, z)$ of the grooves, and the instantaneous position $Z(\theta, t)$ of the free surface, equation (29) becomes a set of ordinary differential equations for the Fourier coefficients of Z, which was solved using VODPK (variable-order preconditioned Krylov) in its explicit integration mode. This ODE integrator is an updated version of the earlier VODE (variable-order ODE integrator) [4].

4.1.3 Regularised equations

As in Hele-Shaw flow with suction, the above model becomes ill-posed in the region of downward moving parts of the interface. We therefore reintroduce the effects of surface tension to suppress numerical instabilities
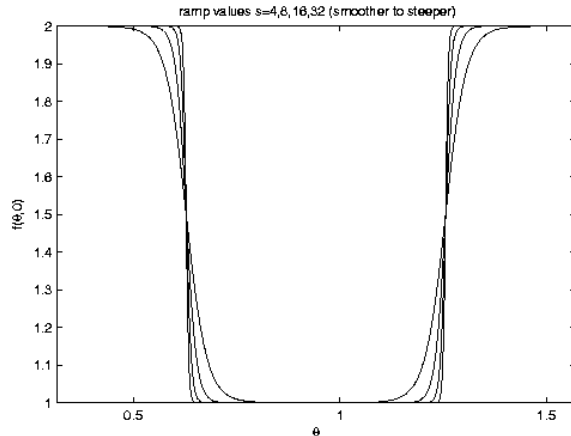
Figure 6: Groove shape given by (32) for $n = H = 2$ and $s = 4, 8, 16, 32$. Larger values of s more closely approximate the square-wave form of the groove considered in the boundary-integral technique used in the next section.

arising from the ill-posedness of the underlying equations. The magnitude of surface tension should not be equated with its true physical value, but rather as a (small) regularising parameter that helps to identify the behavior of the solution in the limit as this parameter tends to zero.

The curvature is given from the formula $\kappa = \nabla \cdot \mathbf{n}$ as

$$\kappa = \nabla \cdot \left(\frac{(-Z_\theta, 1)}{\sqrt{1 + Z_\theta^2}} \right) = -\frac{Z_{\theta\theta}}{(1 + Z_\theta^2)^{3/2}}, \tag{30}$$

so the dynamic boundary condition on $\eta = 1$ becomes

$$p = -\sigma \frac{Z_{\theta\theta}}{(1 + Z_\theta^2)^{3/2}}, \tag{31}$$

with regularisation parameter σ. Since the interface position $Z(\theta, t)$ does not depend on η or z, its derivatives with respect to θ are unaffected by the change of variables in (26). Also by analogy with Hele-Shaw flow, the (much larger) contribution to the total three-dimensional curvature across the narrow gap is taken to be constant, and so just adds a constant offset to the value of atmospheric pressure used at the free surface.

4.1.4 Preliminary Results

As an initial test of this numerical scheme, we simulated the system subject to the groove pattern

$$f(\theta, z) = 1 + \frac{H}{2} \left\{ 1 + \tanh \left[s(\sin \left[n(\theta - kz) \right]) \right] \right\} . \tag{32}$$

Figure 6 shows some examples of this particular groove shape for a fixed value of z with $n = H = 2$. Note that the value of s determines the steepness of the transition from small to large gaps. In all of the runs that follow, there are 256 Fourier modes by 128 grid points in z. A few comparisons with 512×256 simulations suggest that this resolution is adequate provided that the simulation remains stable.

Figure 7 shows the evolution of the interface at two different values of the regularisation parameter $\sigma = 10^{-4}, 5 \times 10^{-5}$, $\alpha = \pi/3$, and $s = 32$. The minimum to maximum gap distance $H = 2$. Note that the development of the an air finger is pronounced over short times, and that the development of this finger is rather insensitive to the size of the regularisation parameter over this time interval. In Figure 8, we consider the same initial values but with different values of the steepness parameter (here $\sigma = 10^{-4}$). Note that the
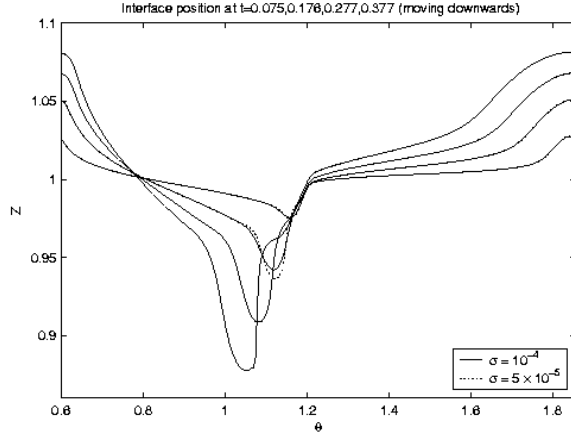
Figure 7: Interfacial dynamics for $\alpha = \pi/3$ and $s = 32$ for two different values of the regularisation parameter $\sigma = 10^{-4}$ and $\sigma = 5 \times 10^{-5}$. Other parameters are $H = 2, n = 5$
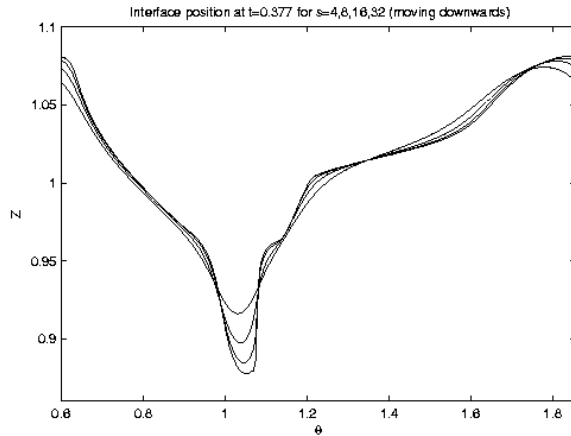
Figure 8: Interfacial dynamics for $\alpha = \pi/3$ and $\sigma = 10^{-4}$ for different values of the steepness parameter $s = 4, 8, 16, 32$. Other parameters are $H = 2, n = 5$

growth of the finger increases with the increase of the steepness parameter. Figure 9 shows the simulation with $\alpha = \pi/4$, $s = 8$, $H = 2, n = 5$ and decreasing the regularisation parameter from $\sigma = 10^{-4}$ to $\sigma = 10^{-5}$. Note how the value of the regularization parameter allows for smaller-scale structures to develop over longer times. Figure 10 considers $\alpha = \pi/5$, with the other values of the parameters the same as in Figure 9. Notice that again the development of the finger is modified by the decrease in the value of the regularisation parameter, but the smaller groove angle results in slower growth of the finger into the lubricating oil. Note that it is not clear from these results if regularisation suppresses overturning since the lubrication model requires the interfacial location to be a single-valued function of θ.

4.2 Boundary-Integral Approach

In typical fluid bearings, the surface of the outer cylinder does not vary smoothly, since it is etched with sharp, spiral grooves. This means that a plausible model for the gap thickness, $f(\theta, z)$, is piecewise constant. Strictly speaking, lubrication theory is not applicable when the topography of the surface varies sufficiently rapidly, and certainly not when f is discontinuous. However, since lubrication theory will be valid away from
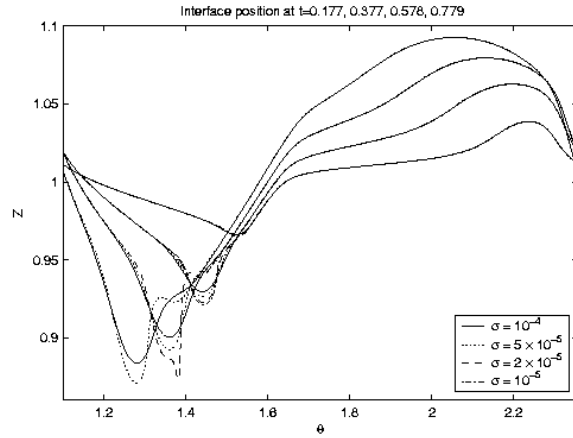
Figure 9: Interfacial dynamics for $\alpha = \pi/4$, $s = 8$, and σ ranging from 10^{-4} to 10^{-5}. Other parameter values are the same as those in 7
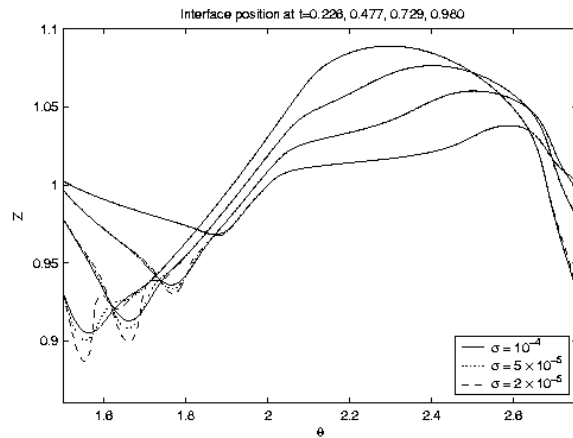
Figure 10: Run for the same parameters as in Figure 9, but with the groove angle $\alpha = \pi/5$.

the discontinuity, it seems reasonable to suppose that we could gain some insight into the structure of the flow by overlooking this theoretical problem. The gain that we make by taking f to be piecewise constant is that Reynolds' equation, (18), becomes Laplace's equation, $\nabla^2 p = 0$, away from the lines of discontinuity. This can be solved using a standard boundary integral technique (see, for example, Pozrikidis [17]), which we will describe below. Before we can proceed, we need to determine appropriate connection conditions along the lines where f is discontinuous.

4.2.1 Lubrication model with grooves

Let $\mathbf{n}_B$ be a unit normal to a line, denoted by B, where f is discontinuous. In integral conservation form, (18) is

$$\int_S f\mathbf{u}.\mathbf{n}_S \, dS = 0 \tag{33}$$

over any region S in the fluid, with outward unit normal $\mathbf{n}_S$. This is valid when f is discontinuous, so we can shrink S into a thin pillbox enclosing the line B. In the limit, we find that

$$[f\mathbf{u} \cdot \mathbf{n}_B] \equiv \left[-\frac{1}{12} f^3 \mathbf{n}_B \cdot \nabla p - \frac{1}{2} f \mathbf{n}_B \cdot \hat{\theta} \right] = 0, \tag{34}$$

where square brackets denote the jump in the enclosed quantity across the line B. Of course, this simply says that flow in equals flow out.

We need another boundary condition at B in order to close the system. An obvious choice is to impose continuity of pressure. However, in reality there may be some loss of pressure as the fluid flows over the step at B. Apart from this, there is a difficulty at the free surface that needs to be addressed. The free surface is advected in the velocity field $\mathbf{u}$ given by (17). Unless $[f^2 \mathbf{n} \cdot \nabla p] = 0$ at the point where the free surface meets B, where $\mathbf{n}$ is a unit normal at the free surface, the velocity field will be discontinuous, which leads to a discontinuity in $Z(\theta, t)$ at B. At first glance, this seems to be supportable, since the free surface would then just follow B at the point of discontinuity in Z. However, we would then need both $p = 0$ and $f^3 \mathbf{n} \cdot \mathbf{u} = 0$ along the line where B and the free surface coincide, which is neither mathematically nor, presumably, physically possible. This difficulty must be associated with the fact that lubrication theory is not valid when f is discontinuous. In order to be able to proceed, we apply the boundary condition

$$[f^2 p] = 0 \tag{35}$$

at B. This forces $[f^2 \mathbf{n} \cdot \nabla p]$ to be continuous at the point where the free surface meets B, since $p = 0$ along the free surface.

We will now assume that the m grooves have constant depth $H > 1$, angular extent θ_0 and make an angle α with the horizontal. This means that we only need to solve in two regions, D_1 where $p \equiv p_1$ and $f = 1$, and D_2, where $p \equiv p_2$ and $f = H$, as shown in figure 11. Both p_1 and p_2 are harmonic, and the initial and boundary conditions are

$$Z(\theta, 0) = Z_{in}(\theta), \tag{36}$$

$$p_i = 0 \quad \text{at } \partial D_i, \tag{37}$$

$$\frac{\partial p_i}{\partial z} = 0 \quad \text{at } z = 0, \tag{38}$$

$$\frac{\partial Z}{\partial t} - \frac{1}{2}\frac{\partial Z}{\partial \theta} = \begin{cases} -\dfrac{1}{12}\dfrac{\partial p_1}{\partial z} & \text{on } \partial D_1, \\[2mm] -\dfrac{1}{12}H^2\dfrac{\partial p_2}{\partial z} & \text{on } \partial D_2, \end{cases} \tag{39}$$

14
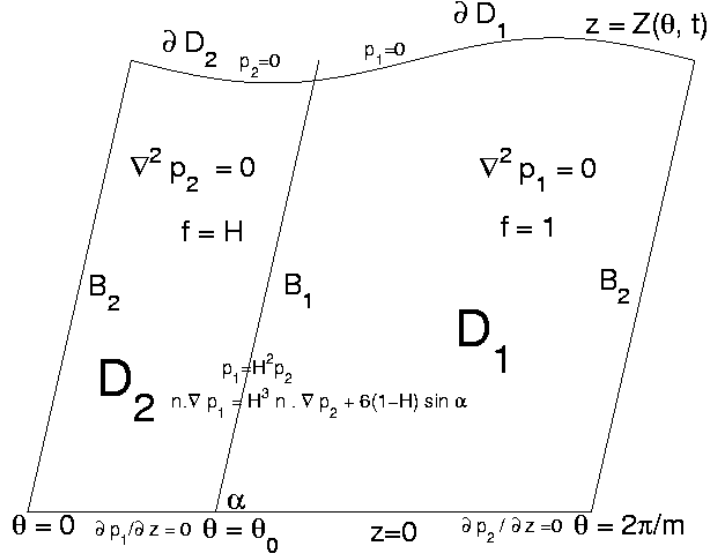
Figure 11: The equations and domains of solution with f piecewise constant.

$$p_1 = H^2 p_2, \quad \mathbf{n}_{B_i} \cdot \nabla p_1 = H^3 \mathbf{n}_{B_i} \nabla p_2 + 6\left(1 - H\right) \mathbf{n}_{B_i} \cdot \hat{\theta} \quad \text{at } B = B_i, \tag{40}$$

for $i = 1, 2$, where ∂D_i is the free surface of D_i and the boundaries B_i are shown in figure 11. The domain is $2\pi/m$-periodic, so that the boundaries marked B_2 in figure 11 can be identified. We must also assume that $Z_{in}(\theta)$ is $2\pi/m$-periodic.

4.2.2 Asymptotic solution for $|H - 1| \ll 1$

Before we discuss the numerical solution of this initial/boundary value problem, we note that there is an asymptotic solution available when $\alpha = \pi/2$, $\delta \equiv H - 1 \ll 1$ and $Z_{in}(\theta) - Z_0 = O(\delta)$ for some $Z_0 > 0$; shallow, axial grooves. We define scaled variables

$$p_i = \delta \hat{p}_i, \quad Z_{in} = Z_0 + \delta \hat{Z}_{in}, \quad Z = Z_0 + \delta \hat{Z}, \tag{41}$$

and assume that $\hat{p}_i$ and $\hat{Z}$ are of $O(1)$ for $\delta \ll 1$. At leading order, the problem defined by (36) to (40) becomes

$$\nabla^2 \hat{p}_2 = 0 \quad \text{for } 0 < \theta < \theta_0, \, 0 < z < Z_0, \tag{42}$$

$$\nabla^2 \hat{p}_1 = 0 \quad \text{for } \theta_0 < \theta < \theta_1 = 2\pi/m, \, 0 < z < Z_0, \tag{43}$$

subject to

$$\hat{p}_i = 0 \quad \text{at } z = Z_0, \tag{44}$$

$$\frac{\partial \hat{p}_i}{\partial z} = 0 \quad \text{at } z = 0, \tag{45}$$

$$\frac{\partial \hat{p}_1}{\partial \theta} - \frac{\partial \hat{p}_2}{\partial \theta} = 6 \quad \text{at } \theta = 0 \text{ and } \theta = \theta_0, \tag{46}$$

15

with $2\pi/m$-periodicity. The solution is easy to obtain as a Fourier series, and we find that

$$\hat{p}_1 = \frac{6}{Z_0} \sum_{k=1}^{\infty} \frac{(-1)^n}{k_n^2 \left(1 - e^{-k_n \theta_1}\right)} \left\{ e^{k_n(\theta - \theta_0 - \theta_1)} - e^{k_n(\theta - \theta_1)} + e^{k_n(\theta - \theta_0)} - e^{-k_n \theta} \right\} \cos k_n z, \tag{47}$$

$$\hat{p}_2 = \frac{6}{Z_0} \sum_{k=1}^{\infty} \frac{(-1)^{n+1}}{k_n^2 \left(1 - e^{-k_n \theta_1}\right)} \left\{ e^{k_n(\theta - \theta_1)} - e^{k_n(\theta - \theta_0)} + e^{-k_n \theta} - e^{-k_n(\theta + \theta_1 - \theta_0)} \right\} \cos k_n z, \tag{48}$$

where

$$k_n \equiv \left(n - \frac{1}{2} \right) \frac{\pi}{Z_0}.$$

From this we can deduce that

$$\hat{Z}(\theta, t) = \hat{Z}_{in}\left(\theta + \frac{1}{2}t\right) + \hat{Z}_{\infty}(\theta) - \hat{Z}_{\infty}\left(\theta + \frac{1}{2}t\right), \tag{49}$$

where $\hat{Z}_{\infty}(\theta)$ is the solution of

$$\frac{d\hat{Z}_{\infty}}{d\theta} = \frac{1}{6} \left. \frac{\partial \hat{p}_i}{\partial z} \right|_{z=0}. \tag{50}$$

We will use this solution below to test that our boundary integral code is working. Note that if $\alpha \neq \pi/2$, the domains of solution are trapeziums rather than rectangles. It may be possible to solve the leading order problem by conformal mapping in this case, but we have not pursued this here.

4.2.3 Numerical solution method

The boundary integral method that we use is similar to that described by Kelly and Hinch [14] for a related Hele-Shaw problem, and is based upon the formulation

$$p_i(s_0) = \frac{1}{\pi} \int_{\partial D^i} \left[\mathbf{n}_i \cdot \nabla p_i(s) \frac{1}{2} \log \left\{ (\Theta(s_0) - \Theta(s))^2 + (Z(s_0) - Z(s))^2 \right\} \right.$$

$$\left. + p_i(s) \frac{\mathbf{n}_i \cdot (\Theta(s_0) - \Theta(s), \ Z(s_0) - Z(s))}{(\Theta(s_0) - \Theta(s))^2 + (Z(s_0) - Z(s))^2} \right] ds, \tag{51}$$

where ∂D^i is the boundary of D_i and its image in the θ-axis, and $\mathbf{n}_i$ is the inward unit normal at ∂D^i. We discretise the boundaries B_1 and B_2 using elements that are logarithmically clustered close to the free surface, and initially uniformly spaced on the free surface, with $Z(\theta, 0) = Z_0$, constant, in all of our simulations. On each element we take $\mathbf{n} \cdot \nabla p_i$ to be constant and p_i to vary linearly. We evaluate the integral in (51) using two point Gaussian quadrature and collocate at the midpoint of each element, calculating the arc length and normal at each element using cubic splines. Along with the boundary conditions (37) at the free surface and (40) at B_1 and B_2, this provides a closed, linear system which we solve at each time step using Gaussian elimination.

We update the position of the free surface using the Lagrangian formulation of the kinematic condition (39),

$$\frac{D\mathbf{X}_j}{Dt} = \mathbf{n}_j \left(\mathbf{u} \cdot \mathbf{n}_j \right) + \mathbf{t}_j u_{tj}, \tag{52}$$

where $\mathbf{n}_j$ and $\mathbf{t}_j$ are the normal and tangent vectors at the free surface marker point $\mathbf{X}_j = (\Theta_j, Z_j)$. In this way, we move each marker point on the free surface in the normal component of the velocity field, whilst allowing some tangential motion with velocity u_s, which does not affect the shape of the free surface. We use

$$u_{tj} = \beta \left(|\mathbf{X}_{j+1} - \mathbf{X}_j| - |\mathbf{X}_j - \mathbf{X}_{j-1}| \right), \tag{53}$$

16
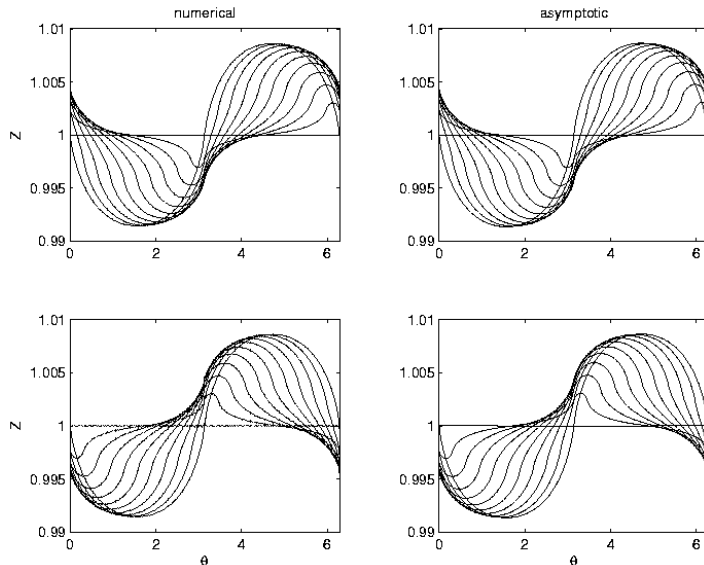
Figure 12: A comparison between the numerical and asymptotic solutions when $H = 1.01$, $Z_0 = 1$, $m = 1$ and $\alpha = \pi/2$. The upper figures show how the solution develops from its initially flat state for $0 \leq t \leq 2\pi$, whilst the lower figures show its relaxation back towards $Z = Z(\theta, 0) = 1$ for $2\pi \leq t \leq 4\pi$.

which effectively puts linear springs between neighbouring marker points. These act to maintain a fairly even spacing. The one exception is that we always advect a marker point on B_1 or B_2 along the discontinuity, so that no marker point crosses from D_1 to D_2 or vice versa. We used $\beta = 100$ in most of the simulations presented below. We solve (52) using Crank-Nicolson time stepping, adjusting the time step so that an iterative procedure converges in less than 5 iterations.

Figure 12 shows a comparison between the numerical and asymptotic solutions for $H = 1.01$, $\alpha = \pi/2$, $\theta_0 = \pi$ and $m = 1$. We used 300 surface grid points and 50 grid points on each of B_1 and B_2. Although some small error is visible when $t = 4\pi$ and the asymptotic solution predicts that $Z = 0$, the agreement is excellent. One notable feature of the solution is that the level of the free surface initially falls in the groove at its right hand edge, as fluid flows into the groove, and rises in the space between, at the left hand edge of the groove, as fluid flows out of the groove (the groove is D_2, the region on the left hand side).

4.2.4 Some numerical solutions

Figure 13 shows the numerical solution for $H = 1.01$, $\alpha = \pi/2$, $\theta_0 = \pi/5$ and $m = 5$. Note that the presence of 5 grooves around the bearing significantly reduces the amplitude of the motion of the free surface compared to the single groove shown in figure 12. This is in line with the results presented earlier for smoothly-varying grooves. Figure 14 shows the numerical solution for $H = 1.01$, $\alpha = \pi/3$ and $m = 5$. The change from axial to spiral grooves has a significant effect on the free surface, breaking the symmetry of the flow.

Unfortunately, for values of H larger than about 1.05, an instability develops on the free surface as it passes across B_1, but interestingly, not as it passes over B_2. Figure 15 illustrates this for $\alpha = \pi/2$, $H = 1.1$, $Z_0 = 1$ and $m = 1$. The instability is grid scale, and appears to be numerical. In order to compute solutions for larger values of H, we introduce some artificial smoothing into the problem by modifying (52) to

$$\frac{D\mathbf{X}_j}{Dt} = \mathbf{n}_j \left(\mathbf{u} \cdot \mathbf{n}_j \right) + \mathbf{t}_j u_{tj} + \bar{\epsilon} \left(\frac{\partial^2 \mathbf{X}}{\partial s^2} \right)_j. \tag{54}$$

We calculate $(\partial^2 \mathbf{X}/\partial s^2)_j$, where s is arc length, using central differences. Note, however, that we do not

17
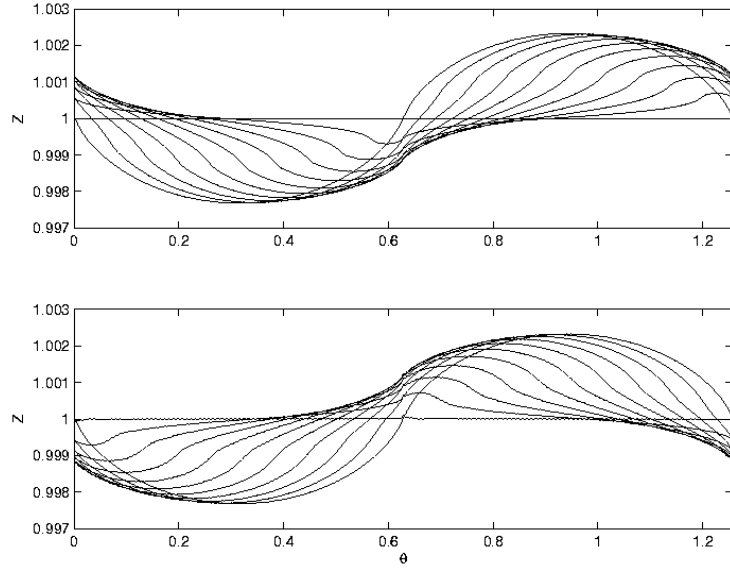
Figure 13: The numerical solution when $H = 1.01$, $Z_0 = 1$, $m = 5$, $\theta_0 = \pi/5$ and $\alpha = \pi/2$. The upper figures show how the solution develops from its initially flat state for $0 \leq t \leq 2\pi/5$, whilst the lower figures show its relaxation back towards $Z = Z(\theta, 0) = 1$ for $2\pi/5 \leq t \leq 4\pi/5$.
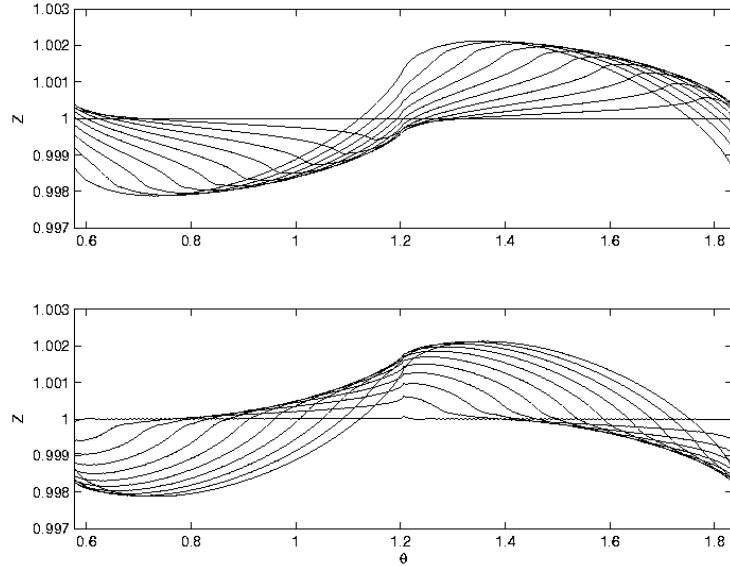
Figure 14: The numerical solution when $H = 1.01$, $Z_0 = 1$, $\theta_0 = \pi/5$, $m = 5$ and $\alpha = \pi/3$. The upper figures show how the solution develops from its initially flat state for $0 \leq t \leq 2\pi/5$, whilst the lower figures show its relaxation back towards $Z = Z(\theta, 0) = 1$ for $2\pi/5 \leq t \leq 4\pi/5$.

18
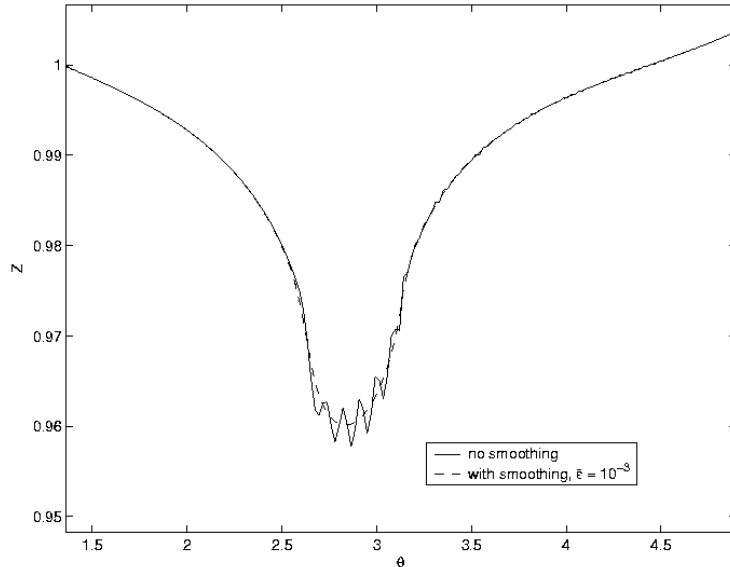
Figure 15: The numerical solution both with and without artificial smoothing when $t = 1$ and $H = 1.1$, $Z_0 = 1$, $m = 1$ and $\alpha = \pi/2$. An instability develops in the unsmoothed solution as the free surface passes over B_1.

apply this correction to the marker points on the lines B_1 and B_2. The positive parameter $\bar{\epsilon}$, an artificial diffusion coefficient, needs to be small. We have taken $\bar{\epsilon} = 10^{-3}$ in the simulations presented below.

This is not the place for an extensive investigation, but we will give a few plots to show the kinds of phenomena that can be observed. We will focus on the case of five grooves ($m = 5$) with a groove of twice the gap width ($H = 2$) and fluid initially of unit height ($Z_0 = 1$), and consider the effect of changing the orientation of the grooves (varying α). As we shall see, small scale features with large curvature develop immediately, so we increase β to 2500. This allows the marker points to adjust rapidly along the free surface and maintain resolution.

The effect of fluid flowing from the gap into the groove is to lower the free surface; a feature that is clearly visible in the previous simulations. Figure 16 shows the solution when $\alpha = \pi/2$. Now that $H = 2$, the flow is fully nonlinear, and the lowering of the free surface almost deforms into a bubble. This feature can also be seen in the simulations with $\alpha = \pi/3$ and $\alpha = \pi/4$, shown in figures 17 and 18. It is not clear why the simulations fail at the times shown, but the solution is very suggestive of bubble formation. When $\alpha = \pi/5$, the surface does not form a bubble, and returns to an almost flat state after one period of the forcing from the grooves, as shown in figure 19.

These results are consistent with the experimental results reported by Asada *et al* [2] . In a five-grooved bearing with grooves of similar depth to the gap width, they reported significant bubble formation when $\alpha = \pi/3$, and no significant bubble formation when $\alpha = \pi/6$ or $\pi/12$.

5   Conclusions

From lubrication theory, we derived a system of equations that describes the pressure field and the interfacial deflections for gap thickness that vary spatially slowly compared to the characteristic gap thickness. This system of equations results in a formulation that can be reduced to that found in Hele-Shaw flow for a fixed gap spacing, and without capillary effects can result in an ill-posed model.

If the variations of the gap thickness are small, the model can be linearized into a Hele-Shaw problem with a forced pressure. For interfacial disturbances that scale on this pressure, the maximum interfacial
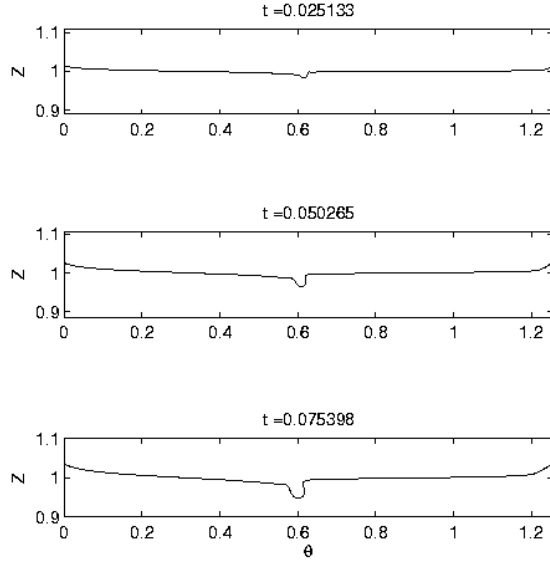
Figure 16: The numerical solution when $H = 2$, $Z_0 = 1$, $\theta_0 = \pi/5$, $m = 5$ and $\alpha = \pi/2$.
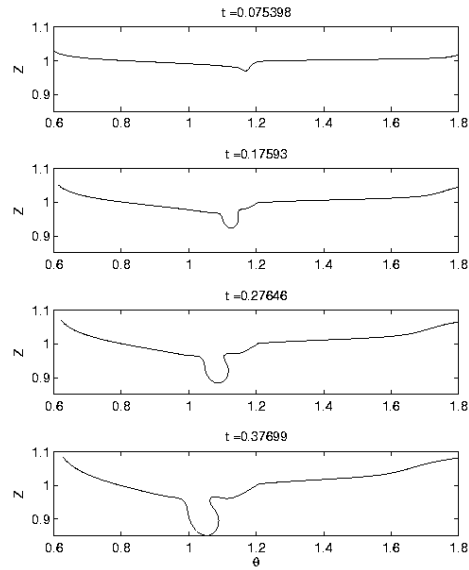
Figure 17: The numerical solution when $H = 2$, $Z_0 = 1$, $\theta_0 = \pi/5$, $m = 5$ and $\alpha = \pi/3$.
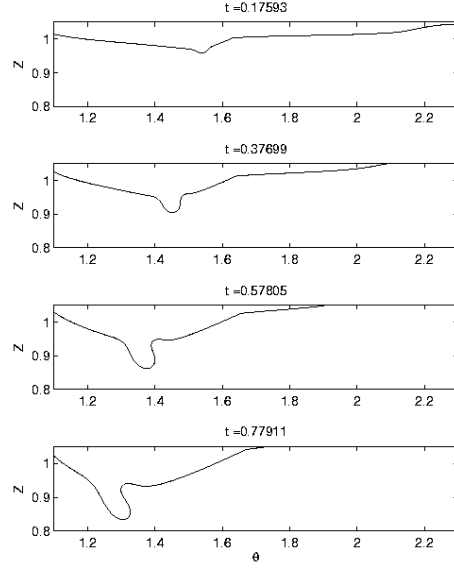
Figure 18: The numerical solution when $H = 2$, $Z_0 = 1$, $\theta_0 = \pi/5$, $m = 5$ and $\alpha = \pi/4$.
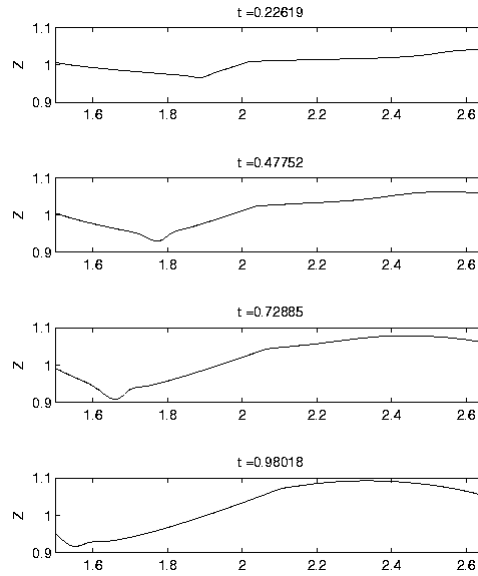
Figure 19: The numerical solution when $H = 2$, $Z_0 = 1$, $\theta_0 = \pi/5$, $m = 5$ and $\alpha = \pi/5$.

deflection decays exponentially with an increasing number of grooves. Further, pressure deviations local to the interface are reduced for sufficiently shallow groove angles. These weaker deviations appear to mitigate instabilities at the interface in the cases studied computationally.

Our first approach was to map the physical domain onto a rectangular computational domain. This mapped problem is then resolved spatially using Fourier modes in the azimuthal coordinate and using finite-difference techniques in the vertical coordinate. From this study, we found that the ill-posedness of the model can be resolved by using the full curvature term in the θ direction. Note that this particular simulation requires that the grooves vary gradually compared to the characteristic gap thickness, but good agreement for steeper groove transitions has been confirmed using a boundary-integral approach.

From this boundary-integral method, we demonstrated that it is possible to simulate the flow in a fluid bearing with piecewise constant gap. A slight doubt hangs over the choice of boundary condition at the lines of discontinuity, which merits further investigation. In addition, the source of the numerical instability described above needs to be investigated. We may simply need to use a more accurate numerical method, and we note that Kelly and Hinch([14]) used six point instead of two-point Gaussian quadrature and quartic rather than cubic splines. Moreover, we have assumed a linear variation of pressure along the boundary elements. However, with all of this in mind, the simulations we have produced give a clear indication that bubbles may be formed at the free surface where the flow enters each groove, if the inclination of the spirals is sufficiently high, as observed in experiment (see ([2])). Note also that, although we have not done so here, it is possible to determine the pressure distribution in the bearing using the boundary integral formulation, through a simple extra calculation once the solution has been obtained.

6 Appendix

6.1 Radial Galerkin Approximation

In this appendix, we consider the Galerkin expansion in y of the kinematic boundary condition given in (10). We expand the interfacial height $Z(\theta, y, t)$ as

$$Z(\theta, y, t) = \bar{Z}(\theta, t)\phi_o(y, f) + \bar{C}(\theta, t)\phi_1(y, f) + \kappa(\theta, t)\phi_2(y, f) \ ,$$

where the orthonormal basis ϕ_o, ϕ_1, ϕ_2 are given by

$$\phi_o(y, f) = \frac{1}{\sqrt{f}} \tag{55}$$

$$\phi_1(y, f) = \sqrt{\frac{12}{f^3}}\left(y - \frac{f}{2}\right) \tag{56}$$

$$\phi_2(y, f) = \sqrt{\frac{720}{f^5}}\left[\frac{y^2}{2} - \frac{yf}{2} + \frac{f^2}{12}\right] \ . \tag{57}$$

We substitute the leading order expressions for $u_{\theta o}, u_{zo}$, and u_{yo} (see (13,14)) along with our ansatz for the interfacial height Z above into the kinematic boundary condition (10). Multiplying the resulting expression by each of the bases ϕ_i and integrating over $y \in (0, f)$ gives us three evolution equations for the

22

coefficients $\bar{Z}, \bar{C}$ and κ,

$$\bar{Z}_t + \left[\frac{1}{12}f^2\frac{\partial p}{\partial \theta} - \frac{1}{2}\right]\bar{Z}_\theta + \frac{1}{24\,f}\left[f^2\frac{\partial p}{\partial \theta} + 6\right]\frac{\partial f}{\partial \theta}\bar{Z} + \frac{\sqrt{3}}{6}\bar{C}_\theta + \frac{\sqrt{5}}{60}f^2\frac{\partial p}{\partial \theta}\frac{\partial \kappa}{\partial \theta}$$

$$-\frac{1}{12f}\left[f^3\nabla^2 p + 2f^2\nabla\cdot(f\nabla p) - 11\frac{\partial f}{\partial \theta} - f^2\frac{\partial p}{\partial \theta}\frac{\partial f}{\partial \theta}\right]\bar{C}$$

$$-\frac{\sqrt{5}}{120f}\left[18f^3\nabla^2 p + 30f^2\nabla\cdot(f\nabla p) - (5f^2\frac{\partial p}{\partial \theta} + 120)\frac{\partial f}{\partial \theta}\right]\kappa = -\frac{1}{12}f^{5/2}\frac{\partial p}{\partial z} \quad (58)$$

$$\bar{C}_t + \frac{\sqrt{3}}{6}\bar{Z}_\theta - \frac{\sqrt{3}}{12\sqrt{f}}\frac{\partial f}{\partial \theta}\bar{Z} + \left(\frac{f^2}{20}\frac{\partial p}{\partial \theta} - \frac{1}{2}\right)\bar{C}_\theta + \sqrt{15}\kappa_\theta$$

$$-\frac{1}{40f}\left\{6f^3\nabla^2 p + 10f^2\nabla\cdot(f\nabla p) - 50\frac{\partial f}{\partial \theta} - 3f^2\frac{\partial p}{\partial \theta}\frac{\partial f}{\partial \theta}\right\}\bar{C}$$

$$-\frac{\sqrt{15}}{60f}\left\{7f^3\nabla^2 p + 12f^2\nabla\cdot(f\nabla p) - 58\frac{\partial f}{\partial \theta} - 3f^2\frac{\partial p}{\partial \theta}\frac{\partial f}{\partial \theta}\right\}\kappa = 0 \quad (59)$$

$$\kappa_t + \frac{\sqrt{5}}{60}f^2\frac{\partial p}{\partial \theta}\bar{Z}_\theta - \frac{\sqrt{5}}{120}f\frac{\partial p}{\partial \theta}\frac{\partial f}{\partial \theta}\bar{Z} + \frac{\sqrt{15}}{15}\bar{C}_\theta - \left[\frac{1}{2} + \frac{5f^2}{84}\frac{\partial p}{\partial \theta}\right]\kappa_\theta$$

$$-\frac{\sqrt{15}}{60f}\left\{f^3\nabla^2 p + f^2\nabla\cdot(f\nabla p) + f^2\frac{\partial p}{\partial \theta}\frac{\partial f}{\partial \theta} + 2\frac{\partial f}{\partial \theta}\right\}\bar{C}$$

$$-\frac{1}{168f}\left[54f^3\nabla^2 p + 84f^2\nabla\cdot(f\nabla p) - 11f^2\frac{\partial p}{\partial \theta}\frac{\partial f}{\partial \theta} - 378\frac{\partial f}{\partial \theta}\right]\kappa = \frac{1}{60}f^{5/2}\frac{\partial p}{\partial z}. \quad (60)$$

Note that in the approximation $\bar{C} = \kappa \equiv 0$, then (58) reduces to (19) if we multiply the resulting equation by $\sqrt{f}$ and combine terms.

6.2 Preliminary Weakly Nonlinear Theory

In this section, we consider the weakly nonlinear analysis of the solution (18,24). We make the following ansatz on the pressure p and the interfacial deflection Z:

$$p = p_o + \delta p_1(\theta, z, t, \tau) + \delta^2 p_2(\theta, z, t, \tau) + \ldots \quad (61)$$

$$Z = A(\tau)Z_{in}(\theta + t/2) + Z_p(\theta) + \delta Z_1(\theta, z, t, \tau) + \delta^2 Z_2(\theta, z, t, \tau) + \ldots, \quad (62)$$

where $\tau = (\alpha_1\delta + \alpha_2\delta^2 + \ldots)t$ is a slow time scale, where the α_i are chosen to remove secular terms in the expansion. If there are no solutions α_i which satisfy these constraints, then a weakly nonlinear solution of this form will not exist.

Applying the ansatz (61),(62) into equations (18, 19) with the form of $f(\theta, z)$ given by (20) gives the following problem for p_1, Z_1:

$$\nabla^2 p_1 = -3\nabla\cdot\{\sin[n(\theta - kz)]\nabla p_o\} \quad (63)$$

$$\frac{\partial Z_1}{\partial t} - \frac{1}{2}\frac{\partial Z_1}{\partial \theta} + \frac{1}{12}\frac{\partial p_1}{\partial \theta} = -\alpha_1 A'(\tau)Z_{in}(\theta + t/2) + \frac{1}{2}\left[A(\tau)Z_{in}(\theta + t/2) + Z_p(\theta)\right]n\cos(n[\theta - k])$$

$$+\frac{1}{12}\sin[n(\theta - k)]\frac{\partial p_o}{\partial z}\bigg|_{z=0} \quad (64)$$

since $\frac{\partial p_o}{\partial \theta}\big|_{z=0} = 0$. Note that secular solutions to the interfacial equation require that all solutions with dependence *only* on the characteristic variable $\xi = \theta + t/2$ must vanish, and so at this order we find that $\alpha_1 = 0$. At the time of this report, this shows that the solution is neutrally stable for times $t = O(1/\delta)$, but the appropriate Landau equation at higher-order in δ will yield the stability criterion for this solution. Although not directly applicable to the system at hand, the criteria which leads to instability for this case should provide insight into the mechanisms for the instability.

References

[1] A.N. Alexandrou and V. Entov. On the steady-state advancement of fingers and bubbles in a Hele-Shaw cell filled by a non-Newtonian fluid. *European J. Appl. Math.*, 8(1):73–87, 1997.

[2] T. Asada, H. Saitou, Y. Asaida, and K. Itoh. Characteristic analysis of hydrodynamic bearings for HDDs. *IEEE Trans. on Magnetics*, 37:810–814, 2001.

[3] F.H. Bark and O. Sundstrom. A note on rotating Hele-Shaw cells. *Journal of Fluid Mechanics*, 111:271–281, 1981.

[4] P.N. Brown, G.D. Byrne, and A. C. Hindmarsh. VODE, a variable-coefficient ODE solver. *SIAM J. Sci. Statist. Comput.*, 10:1038–1051, 1989.

[5] P. Cizek and V. Janovsky. Hele-Shaw flow model of the injection by a point-source. *Proceedings of the Royal Society of Edinburgh Section A*, 91(P1–2):147–159, 1981.

[6] V.M. Entov and P.I. Etingof. Viscous flows with time-dependent free boundaries in a non-planar Hele-Shaw cell. *European J. Appl. Math.*, 8(1):23–35, 1997.

[7] V.M. Entov, P.L. Etingov, and D.Ya. Kleinbock. On nonlinear interface dynamics in Hele-Shaw flows. *European J. Appl. Math.*, 6(5):399–420, 1996.

[8] H.S. Hele-Shaw. The flow of water. *Nature*, 58(1489):33–36, 1898.

[9] Y.E. Hohlov and S.D. Howison. On the classification of solutions to the zero-surface-tension model for Hele-Shaw free-boundary flows. *Quarterly of Applied Mathematics*, 51(4):777–789, 1993.

[10] G.M. Homsy. Viscous fingering in porous media. *Ann. Rev. Fluid Mech.*, 19:271–311, 1987.

[11] S.D. Howison. Cusp development in Hele-Shaw flow with a free surface. *SIAM Journal on Applied Mathematics*, 46(1):20–26, 1986.

[12] S.D. Howison. Fingering in Hele-Shaw cells. *Journal of Fluid Mechanics*, 167:439–453, 1986.

[13] S.D. Howison, A.A. Lacey, and J.R. Ockendon. Hele-Shaw free-boundary problems with suction. *Quarterly Journal of Mechanics and Applied Mathematics*, 41:183–193, 1988.

[14] E.D. Kelly and E.J. Hinch. Numerical simulations of sink flow in the Hele-Shaw cell with small surface tension. *Eur. J. Appl. Math.*, 8:533–550, 1997.

[15] Q. Nie and F.R. Tian. Singularities in Hele-Shaw flows. *SIAM Journal on Applied Mathematics*, 58(1):34–54, 1998.

[16] H. Ockendon and Ockendon J.R. *Viscous flow*. Cambridge University Press, 1995.

[17] C. Pozrikidis. A practical guide to boundary-element methods with the software library bemlib. *Chapman and Hall*, 2002.

[18] S. Richardson. Some Hele-Shaw flows with time-dependent free boundaries. *Journal of Fluid Mechanics*, 102:263–278, 1981.

[19] S. Richardson. Hele-Shaw flows with time-dependent free boundaries in which the fluid occupies a multiply-connected region. *European J. Appl. Math.*, 5:97–122, 1994.

[20] S. Richardson. Hele-Shaw flows with time-dependent free boundaries involving a concentric annulus. *Philosophical Transactions of the Royal Society of London Series A*, 354(1718):2513–2553, 1996.

[21] Y. Saad and M. H. Schultz. GMRES – a generalized minimal residual algorithm for solving nonsymmetric linear systems. *SIAM J. Sci. Statist. Comput.*, 7:856–869, 1985.

[22] M.J. Shelley, F.R. Tian, and K. Wlodarski. Hele-Shaw flow and pattern formation in a time-dependent gap. *Nonlinearity*, 10(6):1471–1495, 1997.

[23] S. Tanveer. The effect of surface-tension on the shape of a Hele-Shaw cell bubble. *Physics of Fluids*, 29(11):3537–3548, 1986.

[24] S. Tanveer. New solutions for steady bubbles in a Hele-Shaw cell. *Physics of Fluids*, 30(3):651–658, 1987.